Electrochimica Acta 439 (2023) 141596

Contents lists available at ScienceDirect

Electrochimica Acta

journal homepage: www.journals.elsevier.com/electrochimica-acta

Surface conductance analysis of X-MoS_2 (X = Fe, Co, Ni) prepared on graphite felt as bifunctional catalysts for the hydrogen/oxidation evolution reactions

Huiyun Shi [a], Youyuan Zhang [a], Ning Pang [a], Shaohui Xu [a,b,*], Dayuan Xiong [a], Lianwei Wang [a], Pingxiong Yang [a], Paul K. Chu [b]

[a] Key Laboratory of Polar Materials and Devices, Ministry of Education, and School of Physics and Electronic Science, East China Normal University, 500 Dongchuan Road, Minhang District, Shanghai 200241, China
[b] Department of Physics, Department of Materials Science & Engineering, and Department of Biomedical Engineering, City University of Hong Kong, Tat Chee Avenue, Kowloon, Hong Kong, China

ARTICLE INFO

Keywords:
Transition-metal-doped MoS_2
HER/OER
Surface adsorption
Surface admittance

ABSTRACT

The surface admittances calculated from electrochemical impedance spectra are used to analyze the surface states of X-MoS_2 (X=Fe, Co, Ni) prepared on graphite felt. Because of the semiconducting properties of Fe-MoS_2 at the electrolyte-semiconductor interface, the bifunctional catalytic properties in the hydrogen/oxidation evolution reactions (HER/OER) are enhanced as a result of better surface adsorption/desorption and slow-changing surface conductance. The surface morphology and electric field between the semiconductor and electrolyte are important parameters affecting the surface properties in HER/OER.

1. Introduction

Water electrolysis is one of the promising methods to produce hydrogen using renewable energy sources such as photovoltaics and wind [1–5]. In the water splitting device, the hydrogen evolution reaction (HER) and oxygen evolution reaction (OER) take place on the two electrodes in an electrolyte. Four electron transfer steps are involved in OER but only two steps occur in HER. For this reason, OER is generally the more sluggish reaction and current research on water electrolysis mainly focuses on the development of high performance, low cost, high natural abundance, environmentally friendly, and stable catalysts in the attempt to replace expensive and scarce precious metals such as Pt and Pd for HER as well as RuO_2 and IrO_2 for OER [1,6]. In addition, there have been a lot of research activities on the design and construction of bifunctional electrocatalysts for both HER and OER in the same electrolyte in order to simplify the hardware and reduce the cost [7–9].

Layered transition-metal dichalcogenides (TMDs) which provide ample paths for carrier transport and more specific surface area than the bulk counterparts have been explored as bifunctional electrocatalysts for overall water splitting [2–4]. MoS_2 is a member of the TMDs family exhibiting promising catalytic activity in HER [6] but not OER in spite of the favorable band alignment in which the valence band edge of monolayer MoS_2 is more positive than the oxidation potential of water. Based on DFT calculation, the poor catalytic OER activity can be ascribed to weak binding between the two key reaction intermediates (hydroxyl and hydroperoxyl) and MoS_2 [10]. Theorical and experimental studies have shown that 3d-transition metals co-doped with six oxygen atoms of MoS_2 (3d-TMO_6@MoS_2, TM = Fe, Mn and Co) have improved OER activity [11]. The hexagonally coordinated transition metals provide the active sites and adsorption-responsive orbitals to enhance adsorption of oxidative intermediates and improve the OER catalytic activity. Further oxidation of Mo edges activates the surface sites resulting in overpotentials comparable to those of the basal surface and S-covered Zig-zig edges [12]. Nanostructured MoS_2 such as nanosheets and quantum dots [13,14] exhibit superior OER activity as a result of exposed MoS_2 basal planes and edge sites on the surface. Therefore, heterostructures formed by MoS_2 together with TMSs and carbonaceous materials are promising OER electrochemical catalysts [15–21]. For example, Pesci and coworkers [17] have observed approximately 1 order of magnitude improvement in the oxygen evolution efficiency from MoS_2/WS_2 on account of better electron-hole separation at the interface of the two materials. Li et al. [19] have

* Corresponding author at: Key Laboratory of Polar Materials and Devices, Ministry of Education, and School of Physics and Electronic Science, East China Normal University, 500 Dongchuan Road, Minhang District, Shanghai 200241, China.
E-mail address: shxu@ee.ecnu.edu.cn (S. Xu).

https://doi.org/10.1016/j.electacta.2022.141596
Received 29 September 2022; Received in revised form 9 November 2022; Accepted 22 November 2022
Available online 23 November 2022
0013-4686/© 2022 Elsevier Ltd. All rights reserved.

synthesized a MoS_2 compound (MoS_2/RGO) on reduced graphene (RGO) by a simple solvothermal method showing an overpotential of 100 mV and Tafel slope of 41 mV dec^{-1} in HER and OER. Fe-doped NiS/MoS_2 [22] has been shown to have abundant interfacial active sites for H- and HO-chemisorption and is a good bifunctional electrocatalyst for HER/OER in 1.0 mol L^{-1} KOH.

Even though it is well known that the surface properties are crucial to the catalytic activity, more fundamental knowledge and understanding are required in order to bring TMS-based catalysts to fruition for commercial electrochemical water splitting. In this respect, electrochemical impedance spectroscopy (EIS) can provide clues about the surface processes [23–29]. EIS data acquired at different temperature and potentials reflect the surface properties and EIS is a valuable tool to analyze the electrolyte-semiconductor and electrolyte-oxide-semiconductor interfaces which may have similar properties as the metal-semiconductor and metal-oxide-semiconductor structures [30]. In this work, a simple one-step hydrothermal method is adopted to prepare transition-metal doped MoS_2 on conductive graphite felt. Electrochemical methods, especially electrochemical impedance spectroscopy, are performed systematically to analyze the effects of different dopants on the catalytic performance of doped MoS_2.

2. Experimental details

2.1. Materials

Sodium molybdate dihydrate ($Na_2MoO_4{\cdot}2H_2O$), thiourea (CSN_2H_4), ferric nitrate hexahydrate ($Fe(NO_3)_3{\cdot}6H_2O$), cobaltous nitrate hexahydrate ($Co(NO_3)_2{\cdot}6H_2O$), nickel nitrate hexahydrate ($Ni(NO_3)_2{\cdot}6H_2O$), concentrated nitric acid (HNO_3, 69%), potassium hydroxide (KOH, >85%), and ethanol (C_2H_6O, 99.5%) were purchased from Sinopharm Chemical Reagent Co. Ltd. The chemicals were analytical grade and used without purification. The aqueous solutions were prepared with ultrapure water (18.2 MΩ cm).

2.2. Synthesis of X-MoS_2@graphite felt (X = Fe, Co, Ni)

The graphite felt (GF) was pretreated using an acid-oxidation method to remove impurities and oil stain. Typically, the 2 cm×4 cm graphite felt was soaked in HNO_3 for one hour at room temperature, washed with deionized water and ethanol successively several times, and vacuum-dried at 60 °C for 8 h.

The metal doped MoS_2 samples were prepared by a one-step hydrothermal method. 1.0 mmol $Na_2MoO_4{\cdot}2H_2O$, 4.0 mmol CSN_2H_4, 0.1 mmol $Fe(NO_3)_3{\cdot}9H_2O$ (or $Co(NO_3)_2{\cdot}6H_2O$ and/or $Ni(NO_3)_2{\cdot}6H_2O$) were dispersed into 20 mL of deionized water and stirred at room temperature. The solution was transferred to a 25 mL Teflon-lined autoclave containing the pretreated graphite felt (GF) and heated to 180 °C for 18 h. After cooling to room temperature, the product was washed with deionized water and ethanol for several times and dried at 60 °C for 8 h to obtain the transition-metal-doped MoS_2 samples designated as Fe-MoS_2@GF, Co-MoS_2@GF, and Ni-MoS_2@GF. For comparison, MoS_2@GF was prepared by the same procedures but without addition of transition metals.

2.3. Materials and electrochemical characterization

The morphology and composition of the samples were characterized by field-emission scanning electron microscopy (FE-SEM, Hitachi S-4800, Japan) and energy-dispersive X-ray spectroscopy (EDS). The surface chemical composition was determined by X-ray photoelectron spectroscopy (XPS) with Al K_α irradiation. Transmission electron microscopy (TEM) was conducted to examine the fine structure and Raman scattering was performed to analyze the vibrational modes using a 514 nm laser.

The electrochemical analysis was carried out using the three-electrode system with 1 mol L^{-1} KOH (Bio-Logic VMP3). The Hg/Hg_2Cl_2 (in saturated KCl) and graphite rod (diameter ~ 0.5 cm) were the reference and counter electrodes, respectively. Cyclic voltammetry (CV) was performed in the potential range between -1.1 and 0.8 V versus SCE at scanning rates between 10 and 100 mV s^{-1}. Linear sweep voltammetry (LSV) was conducted at a scanning rate of 5 mV s^{-1} to assess the HER and OER activity. The reversible hydrogen electrode (RHE) was evaluated according to the following equation:

$$E_{RHE} = E_0 + 0.059pH + E(SCE) \quad (1)$$

where, E_0 is 0.2412 V, pH = 13.6 for 1.0 mol L^{-1} KOH, and E(SCE) is the working voltage (V). The reaction kinetics was evaluated according to the Tafel slope derived from the Tafel plot using the following equation:

$$\eta = b\log|j| + a \quad (2)$$

where, b, η, j, and a are the Tafel slope (mV-dec^{-1}), overpotential (mV), current density (mA-cm^{-2}), and overpotential (V) at 1 mA cm^{-2}, respectively. The electrochemically active area (ECSA) was determined from the electrochemical double layer capacitance (C_{dl}) according to the following equation:

$$ECSA = \frac{C_{dl}}{C_s} \quad (3)$$

where, C_s is the specific capacitance of an atomically smooth surface taken as 40 μF cm^{-2} in 1 mol L^{-1} KOH [31] and C_{dl} was obtained from the △j versus V plot derived from multiple CV scans in a specific voltage range. To calculate the surface admittance, electrochemical impedance spectroscopy (EIS) was performed in the frequency range from 10 mHz to 100 kHz along with an alternating current (AC) bias of 10 mV at the open-circuit potential (OCP) or changing potentials from -1.1 to 0.8 V vs. SCE. All the measurements were performed at room temperature (25 °C) and the results were normalized to the footprint area.

3. Results and discussion

The basic properties of graphite felts (GF) are described in the supporting information. The graphite felt comprises graphite wires with a diameter of about 8 μm and length of several mm as revealed by SEM in Supplementary Fig. S1a (inset). The graphite wires are composed of C and O and a small amount of N as shown in the XPS spectrum in Supplementary Fig. S1a. The ratio of carbon to oxygen is about 4.24. There are defects in the graphite felt as indicated by the significant D-band in the Raman scattering spectra and the intensity ratio of the defect to graphite bands (I_D/I_G) is 0.89 (Supplementary Fig. S1b).

3.1. Structure of X-MoS2@GF (X = Fe, Co, Ni)

Fig. 1 depicts the surface morphologies of MoS_2@GF (1a and 1b), Fe-MoS_2@GF (1c and 1d), Co-MoS_2@GF (1e and 1f), and Ni-MoS_2@GF (1g and 1h) and the EDS spectra are shown in Supplementary Fig. S2. MoS_2@GF consists of a small number of nanoparticles on graphite felt showing a small Mo/S ratio (Supplementary Fig. S2a). The aggregated MoS_2 particles are distributed irregularly (Fig. 1a) on the compact structure (Fig 1b). Fe-MoS_2@GF shows nanoparticles with a diameter of about 400 nm uniformly distributed on the graphite felt (Fig. 1c). The nanoparticles form a layered structure with holes on the rough surface (Fig. 1d). After doping with Fe, The Mo/S ratio increases (Supplementary Fig. S2a). Co-MoS_2@GF shows some spherical structures (Fig. 1e) and agglomeration of the spherical structures produces a compact surface structure (Fig. 1f). Introduction of Co also affects the Mo/S ratio with increasing Mo concentration (Supplementary Fig. S2a). The Ni dopant combines with MoS_2 to form a large number of nanoparticles that cover almost the entire graphite felt (Fig. 1g) and the coverage on GF and compact structure are confirmed by Fig. 1h. EDS further indicates high surface coverage of Ni-MoS_2@GF as reflected by the large

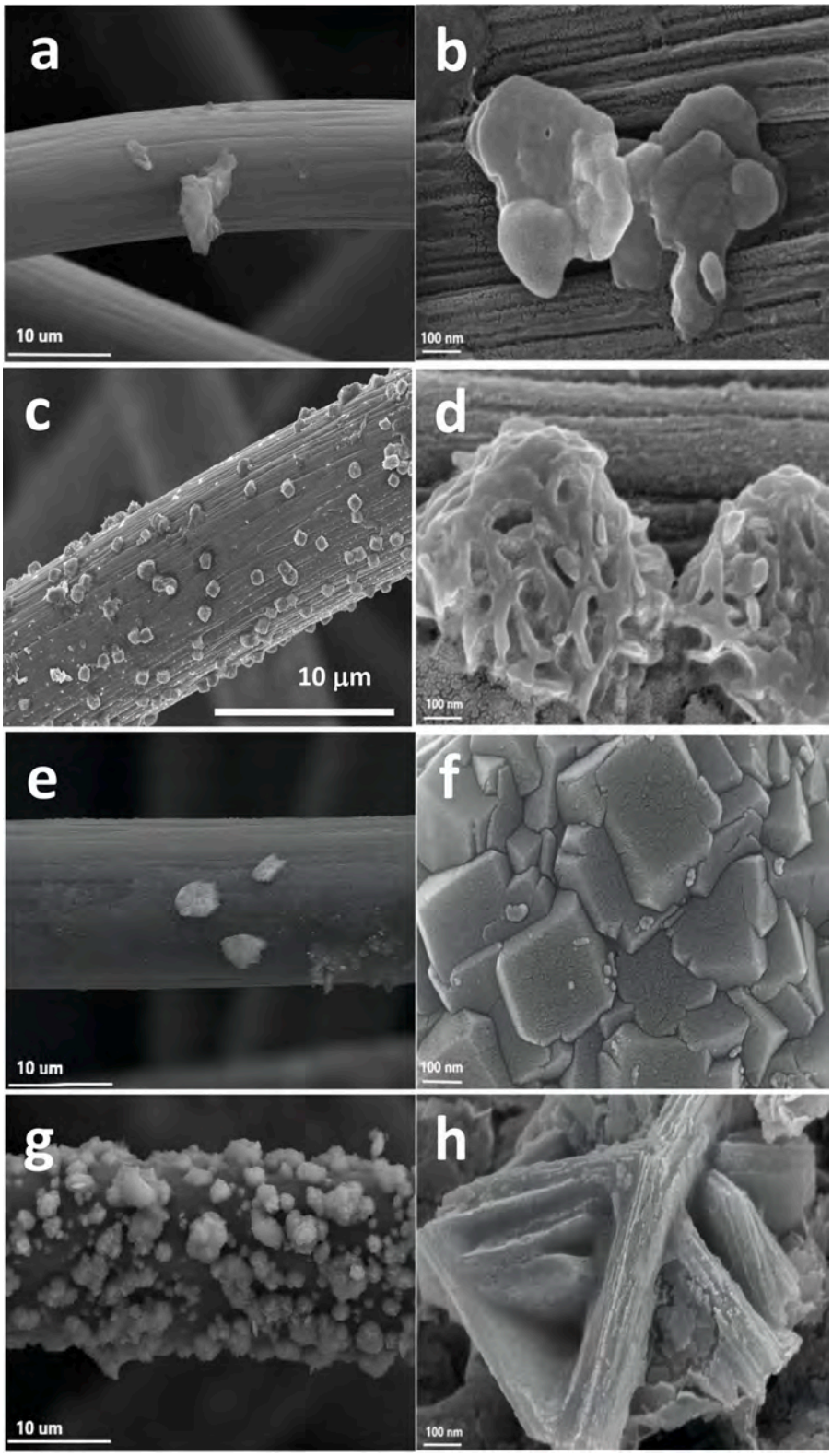

Fig. 1. SEM images of (a, b) MoS_2@GF, (c, d) Fe-MoS_2@GF, (e, f) Co-MoS_2@GF, and (g, h) Ni-MoS_2@GF. The white scale bars in the left and right images are 10 μm and 100 nm, respectively.

Ni, Mo and S peaks and small amounts of C and O (Supplementary Fig. S2a).

The XPS spectra in Fig. 2a reveal C, N and O peaks at 285 eV, 400 eV, and 530 eV, respectively [32], which introduced by the graphite felt and adsorption during the hydrothermal process. Mo and S are detected from all the samples and Fe, Co and Ni are observed from Fe-MoS_2@GF, Co-MoS_2@GF and Ni-MoS_2@GF, respectively. Fig. 2b shows two peaks at 711.4 eV and 725.6 eV for Fe $2p_{1/2}$ and Fe $2p_{3/2}$, respectively, proving that Fe exists in Fe-MoS_2@GF as Fe^{3+} [33]. In addition, owing to the variable valence states of iron, charge transfer and transition between O

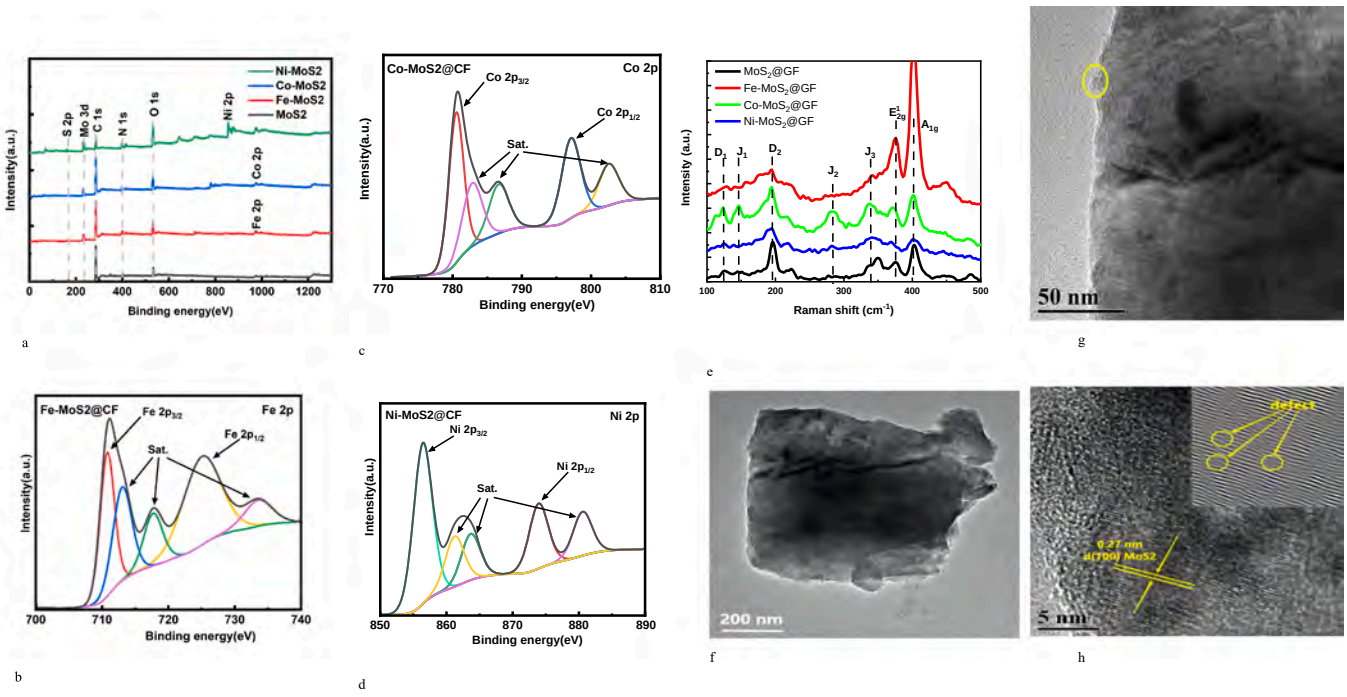

Fig. 2. Surface chemistry and structure of MoS_2@GF and X-MoS_2@GF (X = Fe, Co, Ni): (a) Survey XPS spectra and (b) Fe 2*p*, (c) Co 2*p*, and (d) Ni 2*p* spectra; (e) Raman scattering spectra; (f-h) TEM images of Fe-MoS_2@GF (circle in g is the enlarge region).

2*p* or S 2*p*, and Fe 3*d* form iron oxide or sulfide, peaks of iron compounds are observed at 714.8 eV, 728.8 eV, and 734.2 eV, respectively. Similarly, the peaks at 781.2 and 798.2 eV in the XPS spectrum of Co 2*p* (Fig. 2c) and 854.4 and 874.6 eV in the XPS spectrum of Ni 2*p* (Fig. 2d) are attributed to Co $2p_{1/2}$, Co $2p_{3/2}$, Ni $2p_{1/2}$, and Ni $2p_{3/2}$, respectively [34], confirming the presence of Co^{3+} and Ni^{3+}. The weaker peaks stem from oxide or sulfide impurities of cobalt and nickel. Their exact elemental contents could also be obtained from XPS data, which listed in Supplementary Table S1. It shows the small constituents of Mo (1.19 at %) and S (0.86 at%) elements in MoS_2@GF, comparing to the high ratio of C element (73.1 at%). After doping with Fe element (12.08 at %), the constituents of Mo (20.11 at%) and S (2.46 at%) elements increase in Fe-MoS_2@GF. For Ni-MoS_2@GF, it also indicates the high surface coverage of Ni-MoS_2 corresponding to the high ratio of Ni element (48.36 at%) and low ratio of C element (9.98 at%).

Fig. 2e shows the Raman scattering spectra of MoS_2@GF, Fe-MoS_2@GF, Co-MoS_2@GF, and Ni-MoS_2@GF. The peaks at 380 and 404 cm^{-1} corresponding to the in-plane E^1_{2g} and out-of-plane A_{1g} modes of 2H-phase MoS_2 [35,36] and the three peaks at 146.7, 282 and 338.6 cm^{-1} are the J_1, J_2, and J_3 modes of 1T-phase MoS_2. The Raman spectra of Fe-MoS_2@GF show that 2H-phase MoS_2 is mainly responsible for the intense out-of-plane A_{1g} and in-plane E^1_{2g} modes. For Co-MoS_2@GF, the 1T-phase MoS_2 is the main constituent because that the intensive J_1 and J_2 vibration modes, which would equal to that of the A_{1g} vibration mode [37]. The other samples show the mixed structure of 1T-phase and 2H-phase MoS_2 as reflected by almost the same intensity of the J_1, J_2, and J_3 vibration modes in conjunction with the E^1_{2g} and A_{1g} vibration modes. Raman bands locate at 112 and 197 cm^{-1} (marked as D_1 and D_2) are attributed to the lattice-distorted MoS_2 structure [22], which could also be identified by TEM image. With regard to the metal doped MoS_2, the properties of the semiconductor-electrolyte interface and metallic-electrolyte interface must be explored due to the metallic properties 1T-phase MoS_2 and semiconducting properties 2H-phase MoS_2 [37].

TEM is performed on Fe-MoS_2@GF and Fig. 2f discloses nanospheres with a diameter of about 400 nm and no clearly aggregate is formed throughout the Fe-MoS_2@GF (Fig. 2g). The layered structure consists of layers of MoS_2 nanoflakes (Fig. 2h). The lattice spacing is 0.27 nm which corresponds to the (100) plane of MoS_2 [38]. The inset shows the inverse fast Fourier transform (IFFT) pattern revealing defects and lattice-distorted in Fe-MoS_2@GF.

3.2. *Electrocatalytic activities of X-MoS_2@GF (X = Fe, Co, Ni)*

Fig. 3 shows the hydrogen and oxidation evolution data of X-MoS_2@GF (X = Fe, Co, Ni) in 1.0 mol L^{-1} KOH. Linear sweep voltammetry (Fig. 3a) shows that the overpotential of Fe-MoS_2@GF is 71.3 (119.8) mV for a current density 10 (20) mA cm^{-2}. The overpotentials of Co-MoS_2@GF and Ni-MoS_2@GF are 83.6 and 104.5 mV for a current density 10 mA cm^{-2} and 139.6 and 163.6 mV for a current density 20 mA cm^{-2}, which are much lower than those of the pristine MoS_2@GF (291.9 and 317.8 mV for current density 10 and 20 mA cm^{-2}, respectively). Fig. 3b discloses that the overpotential of Fe-MoS_2@GF is the lowest for both 10 and 20 mA cm^{-2}, which is comparable with the representative reported MoS_2-based catalysts for HER in 1.0 mol L^{-1} KOH solution (Supplementary Table S2).

The Tafel slopes obtained by linear sweep voltammetry are analyzed to elucidate the HER/OER mechanisms and limiting steps. Fig. 3c shows that the Tafel slope of Fe-MoS_2@GF is the smallest (61.6 mV dec^{-1}) compared to Co-MoS_2@GF (89.5 mV dec^{-1}) and Ni-MoS_2@GF (107.1 mV dec^{-1}), while all of them are less than that of the pristine MoS_2@GF (128.1 mV dec^{-1}). The results indicate that the Volmer–Heyrovsky step is the main reaction process on Fe-MoS_2@GF [39]. To evaluate the electrochemical active area (ECSA), cyclic voltammograms are obtained in the narrow potential range between 0.1 and 0.3 V versus RHE at scanning rates from 10 to 100 mV s^{-1} (Supplementary Fig. S3). Fig. 3d shows the current density verse scan rate curves to calculate electrochemical active area (ECSA) according to the double-layer capacitance (C_{dl}). The C_{dl} values of MoS_2@GF, Fe-MoS_2@GF, Co-MoS_2@GF, Ni-MoS_2@GF and GF are 2.31, 6.26, 3.14, 2.93, and 2.23 mF cm^{-2} respectively and the ECSA values are 57.75, 156.5, 78.5 and 73.25, and 55.75 cm^2 respectively.

The OER activity is evaluated in 1.0 mol L^{-1} KOH and Fig. 3e shows

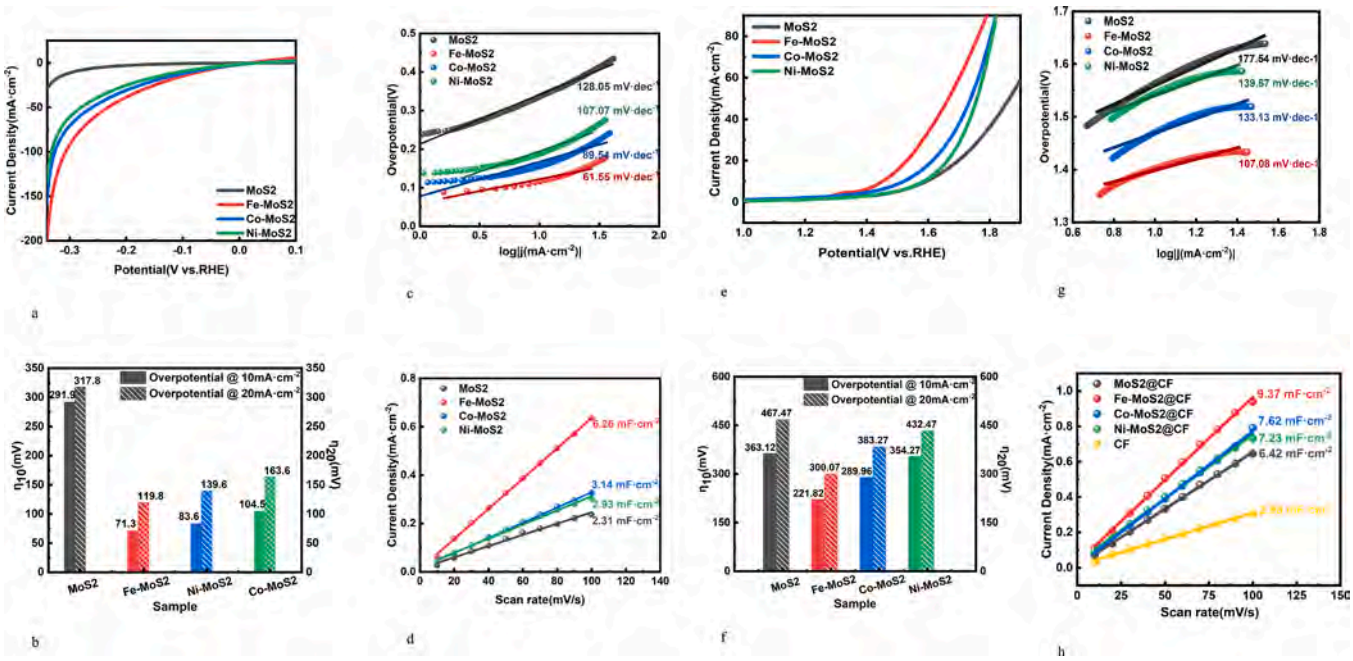

Fig. 3. Electrocatalytic characteristics of MoS_2@GF and X-MoS_2@GF (X = Fe, Co, Ni) in 1 mol L^{-1} KOH: (1) HER characteristics: (a) HER LSV curves, (b) Overpotentials at current densities of 10 and 20 mA cm^{-2}, (c) Tafel plots, and (d) Current-potential curves at different sweeping rates; (2) OER characteristics: (e) OER LSV curves, (f) Overpotentials at current densities of 10 and 20 mA cm^{-2}, (g) Tafel plots, and (h) Current-potential curves at different sweeping rates.

overpotentials of 363.1, 221.82, 289.96, 354.27, and 581.3 mV for a current density 10 mA cm^{-2} for MoS_2@GF, Fe-MoS_2@GF, Co-MoS_2@GF, Ni-MoS_2@GF, and GF, which is comparable with the representative reported MoS_2-based catalysts for OER in 1.0 mol L^{-1} KOH solution (Supplementary Table S3). At a current density 20 mA cm^{-2}, the overpotentials increase to 467.4, 300.1, 383.2, 432.4, and 658.3 mV, respectively. Fig. 3f shows that the overpotential of Fe-MoS_2@GF is the lowest for 10 and 20 mA cm^{-2}. The Tafel slopes of MoS_2@GF, Fe-MoS_2@GF, Co-MoS_2@GF Ni-MoS_2@GF and GF are calculated to be 177.64, 107.08, 133.13, 139.67 mV, and 253.27 mV dec^{-1}, respectively

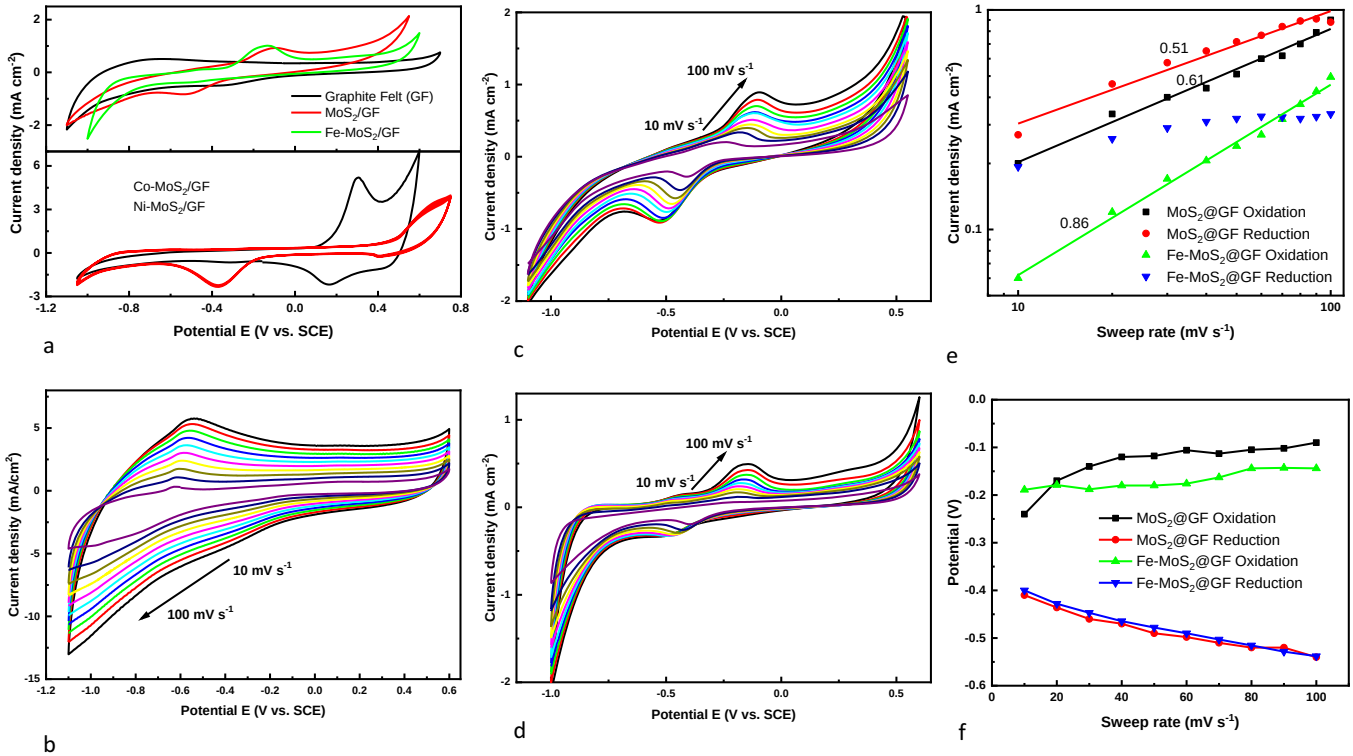

Fig. 4. (a) Cyclic voltammograms of MoS_2@GF and X-MoS_2@GF (X = Fe, Co, Ni) in 1 mol L^{-1} KOH in the potential region between -1.1 V and 0.8 V at a scanning rate of 100 mV s^{-1}; (b) Cyclic voltammograms at scanning rates from 10 to 100 mV s^{-1} acquired from (b) Graphite felt (GF), (c) MoS_2@GF, and (d) Fe-MoS_2@GF; (e) Current densities and (f) Potentials of redox peaks versus scanning rates for MoS_2@GF and Fe-MoS_2@GF.

(Fig. 3g) and Fe-MoS_2@GF shows the smallest Tafel slope value. According to the cyclic voltammograms are obtained in the narrow potential range between 1.1 and 1.3 V versus RHE at scanning rates from 10 to 100 mV s^{-1} (Supplementary Fig. S4), Fig. 3h shows the current density verse scan rate curves to calculate electrochemical active area (ECSA) according to the double-layer capacitance (C_{dl}). It shows that the C_{dl} values of MoS_2@GF, Fe-MoS_2@GF, Co-MoS_2@GF Ni-MoS_2@GF, and GF are 6.42, 9.37, 7.62 7.23, and 2.98 mF cm^{-2} respectively. The corresponding ECSA values are calculated to be 160.5, 234.25, 190.5, 180.75, and 74.5 cm^2, respectively. Owing to a larger active area, the oxygen evolution reaction is enhanced and the results corroborate that doping with transition metals especially Fe improves the OER activity of MoS_2. The Tafel slope shows that rate determining step in OER on Fe-MoS_2@GF is the third step of OH^- adsorption [7]. After proton and electron transfer, the metal oxide adsorbs OH and converts into metal ions and OOH (Such as M-OOH), and then couples with OH^- at the active site to lose an electron and produce oxygen.

3.3. Electrochemical characteristics

Fig. 4a shows the cyclic voltammograms (CV) of X-MoS_2 (X = Fe, Co, Ni) in the potential range from -1.1 to 0.7 V vs. SCE at a scanning rate of 100 mV s^{-1} in 1.0 mol L^{-1} KOH. The CV curve of GF is also shown for comparison. The CV curve of GF shows a square shape in the broad potential range. As the potentials shift to more negative values than -1.1 V vs. SCE, the current density increases steadily due to hydrogen adsorption on GF similar to the electrochemical adsorption on activated carbon [40]. OER occurs at a positive potential of more than 0.7 V. The CV curve of MoS_2@GF shows a clear redox process indicated by the oxidation peak at -0.1 V and reduction peak at -0.5 V. After coating of MoS_2, OER occurs at a small potential of about 0.6 V, while HER is not affected and overlapped with the GF electrode. After doping Fe into MoS_2, the HER potential shifts to about -1.0 V vs. SCE at the low part of Fig. 4a and a larger current density appears at about 0.5 V corresponding to OER.

Cyclic voltammogram (CV) curves are collected at different scanning rates from 10 to 100 mV s^{-1} from graphite felt (Fig. 4b), MoS_2@GF (Fig. 4c), and Fe-MoS_2@GF (Fig. 4d). As shown in Fig. 4b, the CV curves of GF show a square shape and the current density increases with sweeping rates in the broad potential region from -0.4 to 0.6 V corresponding to adsorption of the electrical double layer. Below -0.5 V, the current density increases with scanning rates on account of hydrogen adsorption/desorption on the electrode surface [40]. The anodic (cathodic) peaks of MoS_2@GF (Fig. 4c) shift to the higher (lower) potentials with increasing scanning rates and the currents densities of the anodic and cathodic peaks increase continuously. As for Fe-MoS_2@GF (Fig. 4d), the current densities of the anodic peaks increase continuously with scanning rates and the anodic peaks stay at almost the same potential. The cathodic peaks shift to the lower potentials with scanning rates and the currents densities are almost keep constant, especially at large sweeping rates.

The current densities and potentials of the redox peaks versus scanning rates are shown in Fig. 4e and f, respectively. The potentials of MoS_2@GF shift to positive or negative values with increasing scanning rates and the current densities increase with slope rates of about 0.61 and 0.51 for oxidation and reduction. The potential shift with sweeping rates for anodic and cathodic peak indicates a quasi-reversible redox reaction on MoS_2@GF in KOH [41]. The potentials of the anodic peaks of Fe-MoS_2@GF are almost constant (-0.18 V vs. SCE) and the current densities increase with a slope rate of 0.86. The increasing current densities are related to the surface redox process attributed to surface adsorption. With regard to the cathodic peaks, the potentials shift from -0.4 to -0.53 V continuously with sweeping rate (almost overlapping that of MoS_2@GF). The current densities increase slowly as the scanning rates are increased from 10 to 40 mV s^{-1} and then stabilize (~0.3 mA cm^{-2}) at large sweeping rates (50 to 100 mV s^{-1}).

The changes in the potentials and current densities are related to the semiconducting properties of Fe-MoS_2@GF which comprises 2H-phase MoS_2. A reference potential -0.3 V Vs. SCE is selected corresponding to the meditate value of fast-changing characteristic frequency and surface conductance (see the discussion of surface admittance). At a high potential (oxidized state), n-type MoS_2 remains in the depletion state and the surface field (directed to the electrolyte) enables easier adsorption of negative species such as OH^-. The increasing current densities with scanning rates are associated with the high concentration of OH^- in the solution [6,30,42]. At a small potential (reduced state), n-type MoS_2 stays at the accumulation state and the surface electric field (directed to the MoS_2 electrode) facilitates adsorption of positive species such as H_3O^+ on the electrode surface. The almost constant current density with increasing sweeping rate even at a large potential change stems from the small concentration H^+.

After doping with Co and Ni, metallic properties of MoS_2 are observed from X-MoS_2@GF (X = Co, Ni) and clear redox peaks appear in the potential range between 0.2 and 0.7 V, as shown in Fig. 4a. The CV curves obtained at the different sweeping rates are presented in Supplementary Fig. S5. The quasi-reversed electrochemical process can be inferred from the redox peaks in the CV curves (large potential difference between redox peaks) [41]. The oxidation (reduction) peak of Co-MoS_2@GF at 0.3 (0.18) V vs. SCE corresponds to the electrochemical process between Co^{2+} and Co^{3+} [43] and the oxidation (reduction) peak of Ni-MoS_2@GF at 0.65 (0.4) V vs. SCE represents the electrochemical process between Ni^{2+} and Ni^{3+} [44]. The results indicate that the valence changes affect the surface properties and subsequently the OER and HER performance.

3.4. . Electrochemical impedance spectroscopy

Surface oxidation frequently occurs on semiconductors during immersion in a liquid electrolyte and the oxidation products affect the energy and concentration of surface states in electrochemical processes [23]. In order to better understand the kinetics and charge transfer during HER/OER in 1.0 mol L^{-1} KOH, electrochemical impedance spectra (EIS) are collected at the open-circuit potential (OCP) and Nyquist plots are shown in Fig. 5a and b. Two semicircles in the frequency range from 0.01 to 10,000 Hz appear from MoS_2@GF and X-MoS_2@GF (X = Co, Ni), the equivalent circuit is exhibited in Fig. 5a inset. In the equivalent circuit, the constant phase element (CPE) components are introduced to represent the distribution effects [45] of the three-dimensional (3D) network of GF, and CPE_1 and CPE_2 represent the pseudo-capacitances of the space charge layer and double-layer capacitor corresponding to adsorption, respectively. R_S stands for the series resistance, and R_1 and R_2 are the shunt resistance of the space charge layer and charge transfer resistance in the adsorption process. The agreement between the experimental data (dots) and fitted data (solid) corroborates the validity of the equivalent circuit in the high frequency range from 10^5 to 0.1 Hz. When the frequencies are less than 0.1 Hz, the electrochemical properties are determined by ion diffusion in the solution [45], as also shown the Bode plots of MoS_2@GF and X-MoS_2@GF (X = Fe, Co, Ni) at OCP (Supplementary Fig. S6). The different frequency regions correspond to different electrochemical processes including those at the semiconductor-insulator interface composed of the space charge capacitance C_{SC} (represented by CPE_1) as well as the shunt resistance of the space charge layer R_1 in the high frequency region according to the fast-relaxing element. The capacitance includes the double layer capacitance C_{DL} (represented by CPE_2) and charge transfer resistance of the adsorption process R_2 between the semiconductor and electrolyte in the medium frequencies and diffusion process associated with ions in the solution at low frequencies. The low-frequency response is not analyzed here. In order to study the high-frequency properties, the knee frequency f_N is introduced to distributed the two semicircles, as shown in Fig. 5b. The frequency region higher than f_N corresponds to the space charge layer effect and the lower frequency region represents the

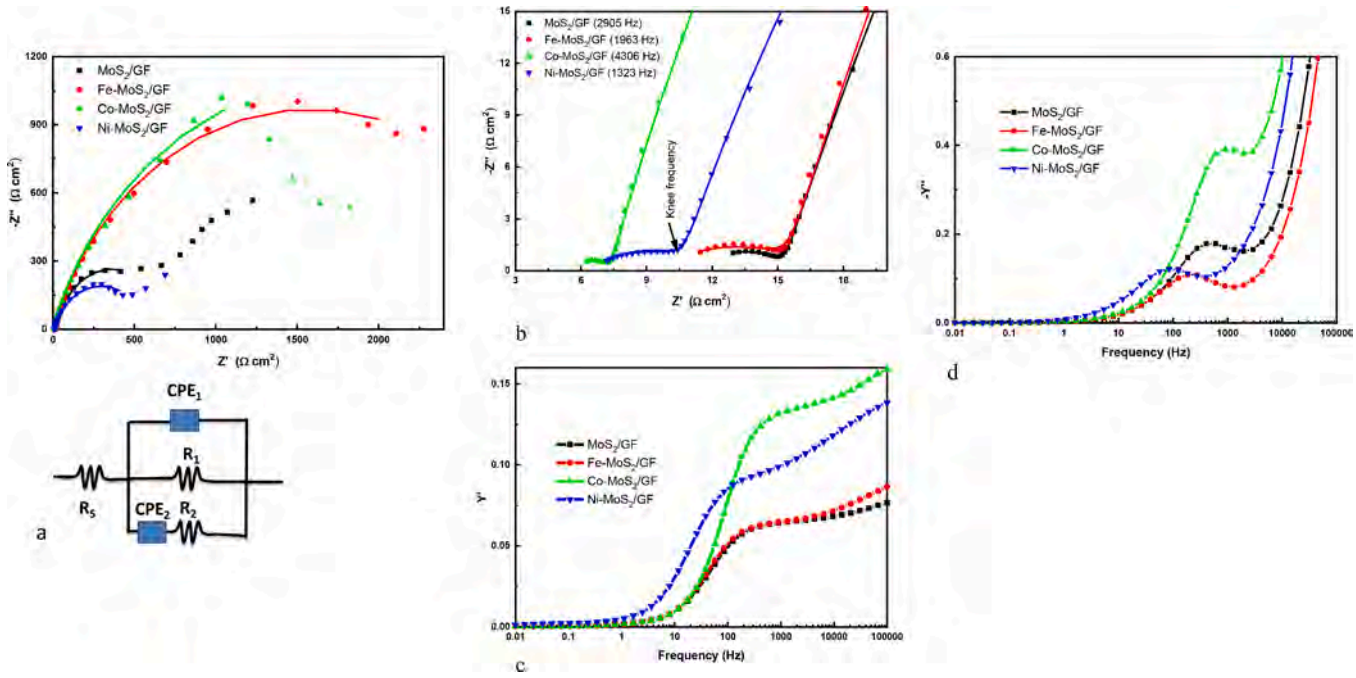

Fig. 5. (a) Impedance Nyquist plots of MoS_2@GF and X-MoS_2@GF (X = Fe, Co, Ni) in 1 mol L^{-1} KOH at the open circuit potential and (b) high frequency region. Inset shows Equivalent circuit. Experimental (dots) and fitted (solid) data. Related surface admittance: (c) Real part and (d) Imaginary part.

adsorption of the electrical double layer. The knee frequency f_N is 1963 Hz for Fe-MoS_2@GF, which lower than that of MoS_2@GF (2905 Hz). The highest knee frequency for Co-MoS_2@GF (4306 Hz) would be attributed to the metallic properties 1T-phase MoS_2 structure. The lowest knee frequency is shown for Ni-MoS_2@GF (1323 Hz) arises from the almost full coverage Ni-MoS_2 on the graphite felt surface.

Table 1 shows that the series resistances R_S are the larger values for Fe-MoS_2@GF (9.64 Ω cm^2) and MoS_2@GF (11.49 Ω cm^2) as a consequence of the semiconducting properties 2H-phase MoS_2. Due to the metallic properties 1T-phase for Co-MoS_2@GF, the smallest series resistance value (5.37 Ω cm^2) and shunt resistance R_1 value (2.3 Ω cm^2) are shown. The small resistances R_S and R_2 of Ni-MoS_2@GF (6.43 and 625 Ω cm^2) is ascribed to large surface coverage of graphite felt and easier adsorption. The fitted constant phase element indicates that the space charge layer effect is consistent due to the nearly unity index n of the constant phase element [45]. In the space charge layer, the indexes n_1 of the constant phase elements are 0.85, 0.87, 0.89, and 0.86 for MoS_2@GF and X-MoS_2@GF (X = Fe, Co, Ni), respectively. In the adsorption process on the electrical double layer, the indexes n_2 of the constant phase elements are almost 0.5 for X-MoS_2@GF (X = Fe, Co, Ni).

If impedance Z subtracts the frequency independence series resistance R_S [24]:

$$Z' = Z - R_S \tag{4}$$

and the resulting admittance can be calculated:

$$Y = \frac{1}{Z'} = \frac{1}{R_1} + \omega^2 \frac{C_{DL2}}{1+\omega^2\tau_2^2} + J\omega\left(C_{SC} + \frac{C_{DL}}{1+\omega_2^{22}}\right) \tag{5}$$

where, $\omega = 2\pi f$ is the angle frequency, $\tau_2 = C_{DL}R_2$ is the relaxation time of the adsorption process. In this case, the contribution of the parallel RC element can be derived by the surface admittance Y. At a given reference potential such as OCP, the surface admittance Y can be determined from the measured impedance data, and the surface admittance comprising the real part Y' identifies the surface electrical conductance and the imaginary part Y'' reflects the characteristic frequency [23,24,28].

$$Y' = \frac{1}{R_1} + \omega^2 \frac{C_{DL2}}{1+\omega^2\tau_2^2} \tag{6}$$

$$Y'' = \omega\left(C_{SC} + \frac{C_{DL}}{1+\omega_2^{22}}\right) \tag{7}$$

Fig. 5 shows the surface admittance of Y' (Fig. 5c) and Y'' (Fig. 5d) as a function of frequencies for MoS_2@GF and X-MoS_2@GF (X = Fe, Co, Ni) in 1 mol L^{-1} KOH. There is a platform (peak) in the real (imaginary) part of surface admittance in the frequency range between 10 and 1000 Hz. Below this frequency range, the real part of surface admittance decreases quickly because the shunt resistance R_1 transfers the current at low frequencies. Above the frequency range, the space charge capacitance C_{SC} is the main parameter corresponding to the increasing imaginary part of surface admittance. The platform (peak) in the middle frequency region is consistent with the frequency of the electrical double layer related to electrochemical adsorption/desorption as shown by the impedance data (Fig. 5b). The judgement of adsorption/desorption process would be confirmed by the surface admittance data of graphite felt (GF) without MoS_2 (Supplementary Figs. S7 and S8). At OCP, the weak platform (peak) appears at about 100–1000 Hz for the real (imaginary) part of the surface admittance (Supplementary Fig. S7) due to the weak adsorption process of GF electrode. For different operation potentials (Supplementary Fig. S8), only in the potential range between

Table 1
Fitted EIS data for MoS_2@GF and X-MoS_2@GF (X = Fe, Co, Ni) in 1.0 mol L^{-1} KOH at the open circuit potential (OCP).

Catalysts	R_S	R_1 (n_1)	R_2 (n_2)	G_{RE}	F_C	N_{it}
MoS_2@GF	11.49	4.0 (0.85)	703 (0.64)	6.3 × 10^{-2}	603.0	2.02 × 10^{12}
Fe-MoS_2@GF	9.64	6.6 (0.87)	3472 (0.50)	6.5 × 10^{-2}	185.5	2.45 × 10^{12}
Co-MoS_2@GF	5.37	2.3 (0.89)	3921 (0.54)	1.3 × 10^{-1}	893.7	5.09 × 10^{11}
Ni-MoS_2@GF	6.43	5.0 (0.86)	625 (0.50)	1.0 × 10^{-1}	84.5	2.21 × 10^{13}

R_S, R_1, R_2: Resistance values (Ω-cm^2), n_1 (n_2): Index of constant phase element, G_{RE}: surface conductance (Ω-cm^2)$^{-1}$, F_C: Characteristic frequency (Hz), N_{it}: surface states (cm^{-2}).

-0.2 V and 0.2 V vs. SCE, the weak platforms (peaks) appear during the frequency region 100–1000 Hz for the real (imaginary) parts of the surface admittance.

The surface conductance can be determined from the real part of the admittance and the frequency of the peak in the imaginary part is related to the characteristic frequency corresponding to the maximum changing rate of surface conductance. The characteristic frequency can be understood as the energy loss associated with the RC circuit and the loss will be maximum when the applied frequency reaches resonance [23]. The capacitance C_i and number of interface states (C_i/e) can be obtained by $R_iC_i = \tau_i$ and $\omega\tau_i = 1$ [23,24], and the related numbers are also shown in Table 1. The surface conductance (platform values) and characteristic frequencies change after incorporation of Fe, Co and Ni into MoS_2. Fe-MoS_2@GF shows a lower surface conductance (6.5×10^{-2} $(\Omega\ cm^2)^{-1}$), lower characteristic frequency (185. 5 Hz), and higher surface state (2.45×10^{12} cm^{-2}). The surface conductance of Co-MoS_2@GF increases to 1.3×10^{-1} $(\Omega\ cm^2)^{-1}$ compared to MoS_2@GF (6.3×10^{-2} $(\Omega\ cm^2)^{-1}$) and Fe-MoS_2@GF, and show a low surface state 5.09×10^{11} cm^{-2} corresponding to the high characteristic frequency 893.7 Hz. Owing to the large coating ratio of Ni-MoS_2@GF, the electrocatalytic properties are not better despite high surface admittance (1.0×10^{-1} $(\Omega\ cm^2)^{-1}$) and surface states (2.21×10^{13} cm^{-2}). It indicates that the surface state of

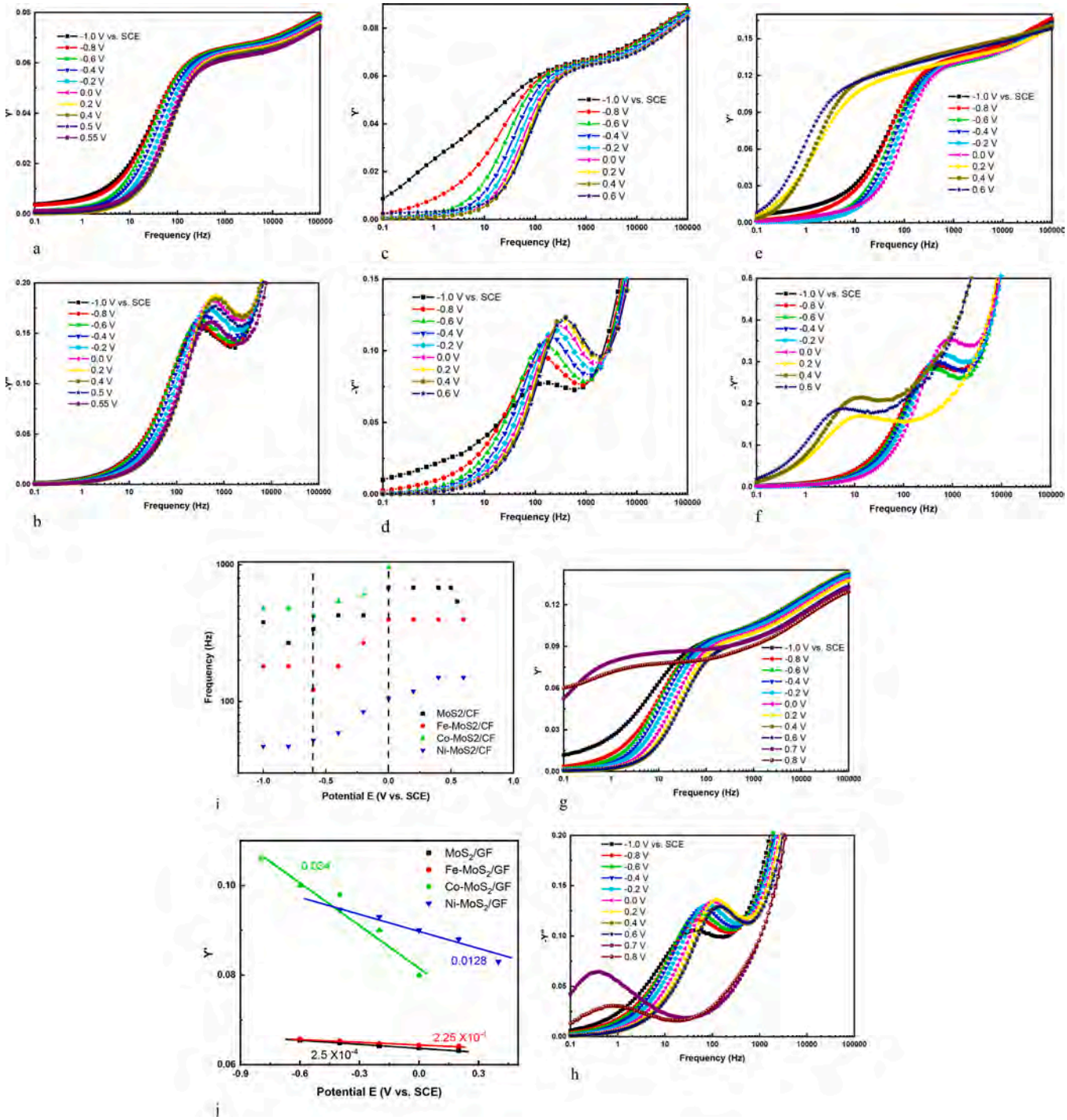

Fig. 6. Surface admittances at the different potentials: (a, b) MoS_2@GF, (c, d) Fe-MoS_2@GF, (e, f) Co-MoS_2@GF, and (g, h) Ni-MoS_2@GF; (i) characteristic frequencies and (j) Surface conductivities.

metal-doped MoS_2 is an important parameter in the electrocatalytic process. The regular nanostructure of Fe-MoS_2 and semiconducting properties render it easier to form the tri-phase interface for improved bifunctional electrocatalytic properties [46].

In order to investigate the adsorption/desorption processes on the electrode surface at different potentials, the real and imaginary parts of the surface admittance are shown in Fig. 6 for MoS_2@GF (6a and 6b), Fe-MoS_2@GF (6c and 6d), Co-MoS_2@GF (6e and 6f), and Ni-MoS_2@GF (6g and 6h). The admittance plateau of MoS_2@GF appears from the frequency range of 10 to 300 Hz, the surface conductance decreases as the potential changes from -1.0 V to 0.4 V (Fig. 6a), and the corresponding characteristic frequencies shift to higher values (Fig. 6b). After Fe doping, the surface conductance decreases steadily in the frequency range from 10 to 500 Hz when the operating potential increases from -1.0 V to 0.6 V (Fig. 6c). With increasing potentials, the characteristic frequencies shift to high values (from 100 to 400 Hz) in the imaginary part of the surface admittance (Fig. 6d). After incorporation of Co, the plateau appears in the frequency range from 10 to 300 Hz and the surface conductance decreases steadily when the operation potential goes up from -1.0 V to 0.0 V (Fig. 6e). With increasing potentials, the characteristic frequencies shift from 400 Hz to 1000 Hz for the imaginary part of the surface admittance (Fig. 6f). When the potential increases from 0.2 to 0.6 V, the plateau of surface conductance and characteristic frequencies shift to low frequencies. The characteristic frequencies shift to 10 Hz at 0.2 V, 8 Hz at 0.4 V and 5 Hz at 0.6 V. The changes of surface conductance and characteristic frequency are related to the surface electrochemical process on Co-MoS_2@GF, as shown by the redox peaks in the CV curve (high potential in Fig. 4a). For Ni-doped MoS_2, the plateau appears at frequencies between 10 and 100 Hz and the surface conductance decreases steadily when the operating potential increases from -1.0 V to 0.6 V (Fig. 6g). The characteristic frequencies shift from 40 Hz to 100 Hz in the imaginary part of the surface admittance (Fig. 6h). At a potential higher than 0.6 V, the plateau of the surface conductance and the characteristic frequencies shift to low frequencies, 0.3 Hz at 0.7 V and 0.7 Hz at 0.8 V. The change of surface conductance is associated with the surface electrochemical process of Ni-MoS_2@GF as shown by the redox peaks in the CV curves (Fig. 4a).

In order to analyze the change of the surface admittance with potentials quantitatively, the characteristic frequency and surface conductance are summarized in Fig. 6i and j, respectively. The characteristic frequencies increase with potentials, and the large frequency increasing appear during the potential region between -0.6 and 0 V vs. SCE (dashed lines in Fig. 6i). The medium frequency (-0.3 V vs. SCE) would be selected to distributed two parts of the potential region corresponding to the different surface process, as discussed in CV curves. The characteristic frequency of Fe-MoS_2@GF increases by almost 3.3 times from 120 to 400 Hz when the operating potential increases from -0.6 to 0 V, corresponding to large changing of surface states for adsorption/desorption process. The characteristic frequencies of MoS_2@GF and Co-MoS_2@GF increase by 2 times (from 338 to 680 Hz) and 2.2 times (from 430 to 960 Hz), respectively. Ni-MoS_2@GF shows the low characteristic frequencies and increase from 52 to 105 Hz (2 times) when the operating potential goes up from -0.6 to 0 V.

The surface conductance decreases linearly with potentials from -0.8 to 0.4 V vs. SCE, as shown in Fig. 6j. Fe-MoS_2@GF shows the smallest decreasing rate of 2.25×10^{-4} in comparison with MoS_2@GF (2.5×10^{-4}). Co-MoS_2@GF shows a largest decreasing rate of 0.034. It indicates that bifunctional electrocatalytic properties would determine by surface adsorption/desorption process and the changing of surface conductance with potential. For semiconductor properties of Fe-MoS_2@GF, it shows the large quantity of surface adsorption/desorption and slow-changing surface conductance, and excellent bifunctional electrocatalytic properties are achieved. The fast-changing surface conductance and small adsorption/ desorption quantity would be related to the metallic properties of Fe-MoS_2@GF. Large adsorption/desorption quantity (2.21×10^{13} cm^{-2}) and fast-changing rate of surface admittance (0.013) are observed from Ni-MoS_2@GF. However, the performance in bifunctional electrocatalysis stems from the inefficient tri-phase interface of Ni-MoS_2@GF due to the large surface coverage of Ni-MoS_2 on graphite felt.

4. Conclusion

A one-step hydrothermal method is adopted to prepare transition-metal-doped MoS_2 on conductive graphite felt. Electrochemical assessment and surface admittance analysis based on electrochemical impedance spectroscopy are carried out to investigate the surface states of X-MoS_2 (X = Fe, Co, Ni). Owing to the semiconducting properties of Fe-MoS_2, surface adsorption/desorption, as well as slow-changing surface conductance with operating potentials, excellent bifunctional electrocatalytic properties are achieved. The electrochemical properties can be explained based on the surface electric field between the semiconductor and electrolyte at different potentials. The results indicate that the surface morphology and electric field are crucial to the characteristics and stability of the bifunctional electrode in HER/OER.

CRediT authorship contribution statement

Huiyun Shi: Methodology, Investigation, Writing – original draft. **Youyuan Zhang:** Methodology, Investigation. **Ning Pang:** Methodology, Investigation. **Shaohui Xu:** Writing – review & editing, Supervision, Project administration. **Dayuan Xiong:** Project administration, Funding acquisition. **Lianwei Wang:** Supervision, Project administration, Funding acquisition. **Pingxiong Yang:** Project administration, Writing – review & editing. **Paul K. Chu:** Writing – review & editing, Funding acquisition.

Declaration of Competing Interest

The authors declare that they have no known competing financial interests or personal relationships that could have appeared to influence the work reported in this paper.

Acknowledgments

This work was jointly supported by National Natural Science Foundation of China (No. 61176108), Research Innovation Foundation of ECNU (No. 78210245), City University of Hong Kong Donation Research Grant (DON-RMG, No. 9229021), and City University of Hong Kong Strategic Research Grant (SRG, No. 7005505).

Supplementary materials

Supplementary material associated with this article can be found, in the online version, at doi:10.1016/j.electacta.2022.141596.

References

[1] J. Wang, Y. Gao, H. Kong, et al., Non-precious-metal catalysts for alkaline water electrolysis: operando characterizations, theoretical calculations, and recent advances, Chem. Soc. Rev. 49 (2020) 9154–9196.
[2] Q. Fu, J. Han, X. Wang, et al., 2D transition metal dichalcogenides: design, modulation, and challenges in electrocatalysis, Adv. Mater. 33 (2021), 1907818 (1 to 24).
[3] C. Das, N. Sinha, P. Roy, Transition metal non-oxides as electrocatalysts: advantages and challenges, Small 18 (2022), 2202033 (1 to 67).
[4] X. Wu, H. Zhang, J. Zhang, X. Lou, Recent advances on transition metal dichalcogenides for electrochemical energy conversion, Adv. Mater. 33 (2021), 2008376 (1 to 24).
[5] H. Sun, Z. Yan, F. Liu, et al., Self-supported transition-metal-based electrocatalysts for hydrogen and oxygen evolution, Adv. Mater. 32 (2020), 1806326 (1 to 18).
[6] Y. Cao, Roadmap and direction toward high-performance MoS_2 hydrogen evolution catalysts, ACS Nano 15 (2021) 11014–11039.
[7] M. Wang, L. Zhang, Y. He, H. Zhu, Recent advances in transition-metal-sulfide-based bifunctional electrocatalysts for overall water splitting, J. Mater. Chem. A 9 (2021) 5320–5363.

[8] I.S. Amiinu, Z. Pu, X. Liu, K.A. Owusu, et al., Multifunctional Mo-N/C@MoS_2 electrocatalysts for HER, OER, ORR, and Zn-air batteries, Adv. Funct. Mater. 27 (2017), 1702300 (1 to 11).

[9] M. Kumar, T.C. Nagaiah, A multifunctional cobalt iron sulfide electrocatalyst for high performance Zn-air batteries and overall water splitting, J. Mater. Chem. A 10 (2022) 4720–4730.

[10] E. German, R. Gebauer, Why are MoS_2 monolayers not a good catalyst for the oxygen evolution reaction? Appl. Surf. Sci. 528 (2020), 146591 (1 to 7).

[11] N. Ran, E. Song, Y. Wang, et al., Dynamic coordination transformation of active site in single-atom MoS_2 catalyst for boosted oxygen evolution catalysis, Energy Environ. Sci. 15 (2022) 2071–2083.

[12] H. He, H. Chen, J. Chen, et al., Dual sites modulating MoO_2 nanospheres for synergistically enhanced electrocatalysis of water oxidation, Chem. Eng. J. 443 (2022), 136339 (1 to 7).

[13] Z. Sadighi, J. Liu, L. Zhao, et al., Metallic MoS_2 nanosheets: multifunctional electrocatalyst for the ORR, OER and Li-O_2 batteries, Nanoscale 10 (2018) 22549–22559.

[14] B. Mohanty, M. Ghorbani-Asl, S. Kretschmer, et al., MoS_2 quantum dots as efficient catalyst materials for the oxygen evolution reaction, ACS Catal. 8 (2018) 1683–1689.

[15] J. Zhang, T. Wang, D. Pohl, et al., Interface engineering of MoS_2/Ni_3S_2 heterostructures for highly enhanced electrochemical overall-water-splitting activity, Angew. Chem. Int. Ed. 55 (2016) 6702–6707.

[16] Y. Yang, H. Yao, Z. Yu, S.M. Islam, et al., Hierarchical nanoassembly of MoS_2/Co_9S_8/Ni_3S_2/Ni as a highly efficient electrocatalyst for overall water splitting in a wide pH range, J. Am. Chem. Soc. 141 (2019) 10417–10430.

[17] F.M. Pesci, M.S. Sokolikova, C. Grotta, et al., MoS_2/WS_2 heterojunction for photoelectrochemical water oxidation, ACS Catal. 7 (2017) 4990–4998.

[18] Y. Li, Z. Yin, M. Cui, X. Liu, et al., Interface engineering of transitional metal sulfide-MoS_2 heterostructure composites as effective electrocatalysts for water-splitting, J. Mater. Chem. A 9 (2021) 2070–2092.

[19] Y. Li, H. Wang, L. Xie, et al., MoS_2 nanoparticles grown on graphene: an advanced catalyst for the hydrogen evolution reaction, J. Am. Chem. Soc. 133 (2011) 7296–7299.

[20] H. Yu, Y. Xue, L. Hui, C. Zhang, et al., Controlled growth of MoS_2 nanosheets on 2D N-doped graphdiyne nanolayers for highly associated effects on water reduction, Adv. Funct. Mater. 28 (2018), 1707564 (1 to 8).

[21] L. Ma, L. Jiang, X. Li, P. Zuo, et al., One-step ultrafast laser induced synthesis of strongly coupled 1T-2H MoS_2/N-rGO quantum-dot heterostructures for enhanced hydrogen evolution, Chem. Eng. J. 445 (2022), 136618 (1 to 12).

[22] J. Tian, X. Xing, Y. Sun, X. Zhang, et al., Strongly coupled Fe-doped NiS_2/MoS_2 composite for high-efficiency water splitting, Chem. Commun. 58 (2022) 557–560.

[23] E. Barsoukov, J.R. Macdonald, Impedance Spectroscopy Theory, Experiment, and Applications, Second Edition, John Wiley & Sons, Inc., Hoboken, New Jersey, 2005.

[24] J.L. Diot, J. Joseph, J.R. Matin, P. Clechet, pH dependence of the Si/SiO_2 interface state density for EOS systems, Electroanal. Chem. 193 (1985) 75–88.

[25] M.C.A. Fantini, W.M. Shen, M. Tomkiewicz, J.P. Gambino, Liquid junctions for characterization of electronic materials. I. The potential distribution at the Si/methanol interface, J. Appl. Phys. 65 (1989) 4884–4890.

[26] M.C.A. Fantini, W.M. Shen, M. Tomkiewicz, J.P. Gambino, Liquid junctions for characterization of electronic materials. IV. Impedance spectroscopy of reactive ion-etched Si, J. Appl. Phys. 66 (1989) 2148–2155.

[27] W.M. Shen, M. Tomkiewicz, D. Sedaries, C. Levy-Clement, Photoreflectance and impedance study of InSe and modified InSe, J. Electroch. Soc. 137 (1990) 2656–2661.

[28] A.C. Meng, K. Tang, M.R. Braun, L. Zhang, P.C. McIntyre, Electrochemical impedance spectroscopy for quantitative interface state characterization of planar and nanostructured semiconductor-dielectric interfaces, Nanotechnology 28 (2017), 415704 (1 to 10).

[29] B. Miao, K. Sangare, A. Iqbal, B. Marsan, K.H. Bevan, Interpreting interfacial semiconductor-liquid capacitive characteristics impacted by surface states: a theoretical and experimental study of $CuGaS_2$, Phys. Chem. Chem. Phys. 22 (2020) 19631–19642.

[30] S.M. Sze, Physics of Semiconductor Devices, Second Edition, John Wiley and Sons, New York, 1981.

[31] Y. Yoon, B. Yan, Y. Surendranath, Suppressing ion transfer enables versatile measurements of electrochemical surface area for intrinsic activity comparisons, J. Am. Chem. Soc. 140 (2018) 2397–2400.

[32] Y. Yan, S. Liang, X. Wang, et al., Robust wrinkled MoS_2/N-C bifunctional electrocatalysts interfaced with single Fe atoms for wearable zinc-air batteries, Proc. Natl. Acad. Sci. USA 118 (2021), e211003611 (1 to 8).

[33] Y. Chen, Z. Li, Y. Zhu, et al., Atomic Fe dispersed on N-doped carbon hollow nanospheres for high-efficiency electrocatalytic oxygen reduction, Adv. Mater. 31 (2019), 1806312 (1 to 8).

[34] W. Zhao, S. Yuan, L. Zhang, et al., Engineering metal-sulfides with cations-tunable metal-oxides electrocatalysts with promoted catalytic conversion for robust ions-storage capability, Energy Storage Mater. 45 (2022) 1183–1200.

[35] G.L. Frey, R. Tenne, M.J. Matthews, et al., Raman and resonance Raman investigation of MoS_2 nanoparticles, Phys. Rev. B 60 (1990) 2883–2892.

[36] K. Zhou, F. Withers, Y. Cao, S. Hu, et al., Raman modes of MoS_2 used as fingerprint of van der Waals interactions in 2-D crystal-based heterostructures, ACS Nano 8 (2014) 9914–9924.

[37] X. Geng, W. Sun, W. Wu, et al., Pure and stable metallic phase molybdenum disulfide nanosheets for hydrogen evolution reaction, Nat. Commun. 7 (2016) 10672 (1–7).

[38] J. Gong, Z. Zhang, Z. Zeng, et al., Graphene quantum dots assisted exfoliation of atomically-thin 2D materials and as-formed 0D/2D van der Waals heterojunction for HER, Carbon 184 (2021) 554–561.

[39] B.E. Conway, B.V. Tilak, Interfacial processes involving electrocatalytic evolution and oxidation of H_2, and the role of chemisorbed H, Electrochim. Acta 47 (2002) 3571–3594.

[40] K. Fic, M. Meller, E. Frackowiak, Interfacial redox phenomena for enhanced aqueous supercapacitors, J. Electrochem. Soc. 162 (2015) A5140–A5147.

[41] A.J. Bard, R. Larry, Electrochemical Methods: Fundamentals and Applications, John Wiley & Sons, Inc, New York, 2001.

[42] A. Hankin, F.E. Bedoya-Lora, J.C. Alexander, et al., Flat band potential determination: avoiding the pitfalls, J. Mater. Chem. A 7 (2019) 26162–26176.

[43] M. Li, S. Xu, Y. Zhu, P. Yang, et al., Heterostructured $Ni(OH)_2$-$Co(OH)_2$ composites on 3D ordered Ni-Co nanoparticles fabricated on microchannel plates for advanced miniature supercapacitor, J. Alloy. Compd. 589 (2014) 364–371.

[44] G. Barral, F. Njanjo-Eyoke, S. Maximovitch, Characterization of the passive layer and of hydroxide deposits of nickel by impedance spectroscopy, Electrochim. Acta 40 (1995) 2815–2828.

[45] M.E. Orazem, B. Tribollrt, Electrochemical Impedance Spectroscopy, John Wiley & Sons, Inc, New Jersey, Hoboken, 2008.

[46] S.B. Adler, Factors governing oxygen reduction in solid oxide fuel cell cathodes, Chem. Rev. 104 (2004) 4791–4843.

Surface conductance analysis of X-MoS_2 (X = Fe, Co, Ni) prepared on graphite felt as bifunctional catalysts for the hydrogen/oxidation evolution reactions

Huiyun Shi[a], Youyuan Zhang[a] , Ning Pang[a], Shaohui Xu[a,b*], Dayuan Xiong [a], Lianwei Wang[a], Pingxiong Yang[a], and Paul K. Chu[b]

[a] Key Laboratory of Polar Materials and Devices, Ministry of Education, and School of Physics and Electronic Science, East China Normal University, 500 Dongchuan Road, Minhang District, Shanghai, 200241, China

[b] Department of Physics, Department of Materials Science & Engineering, and Department of Biomedical Engineering, City University of Hong Kong, Tat Chee Avenue, Kowloon, Hong Kong, China.

*Author to whom correspondence should be addressed. Electronic mail: **shxu@ee.ecnu.edu.cn** (Shaohui Xu); Tel.: +86 21 54342501; Fax: +86 21 54345119

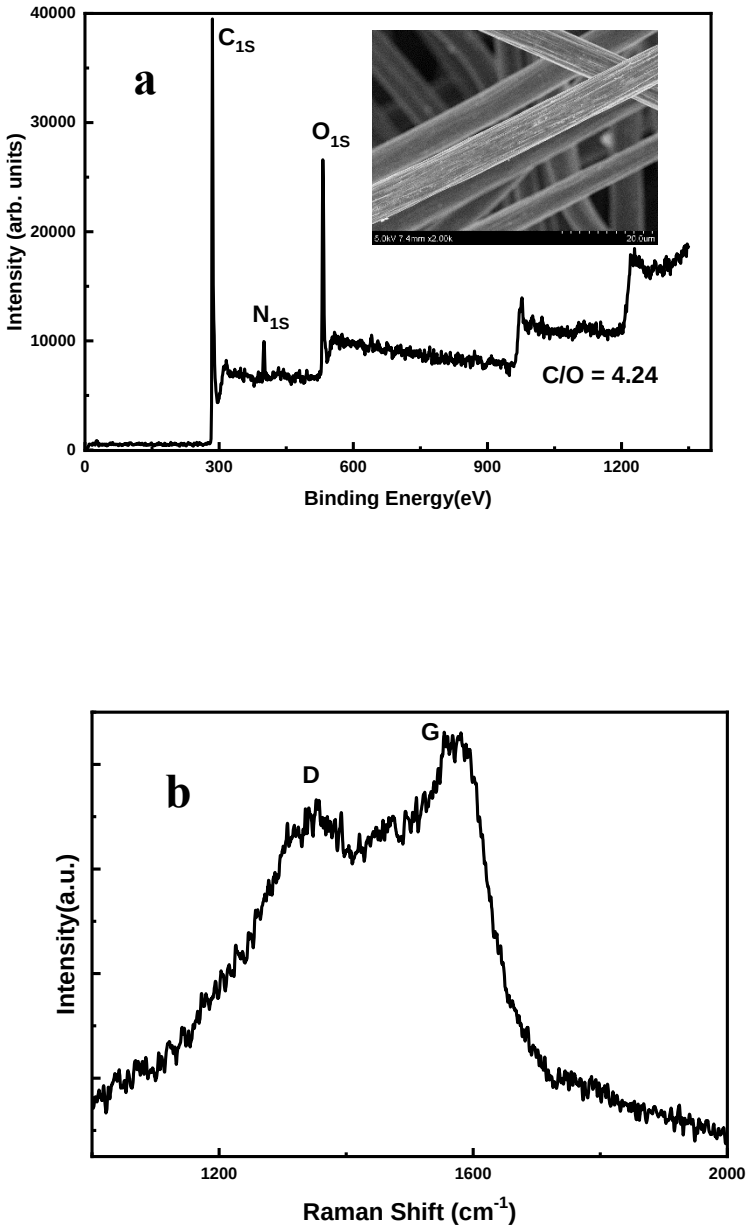

Figure S1. (a) XPS spectrum and (b) Raman scattering spectrum of graphite felt. Inset in (a) shows the SEM image.

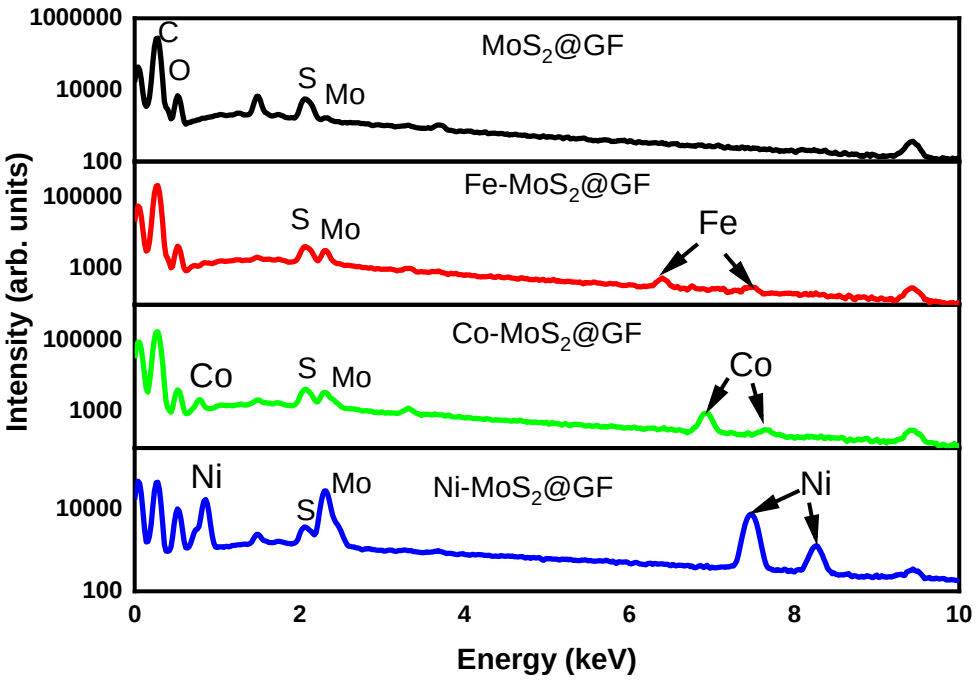

Figure S2. EDS spectra of MoS_2@GF and X-MoS_2@GF (X = Fe, Co, Ni).

Table S1 Element ration (at%) of X-MoS_2 (X = Fe, Co, Ni) based on XPS data.

	C	O	Mo	S	Metal
MoS_2@GF	73.15	24.80	1.19	0.86	
Fe-MoS_2@GF	44.08	21.25	20.11	2.46	12.08
Co-MoS_2@GF	42.91	24.09	10.83	0.45	21.72
Ni-MoS_2@GF	9.98	25.84	15.26	0.56	48.36

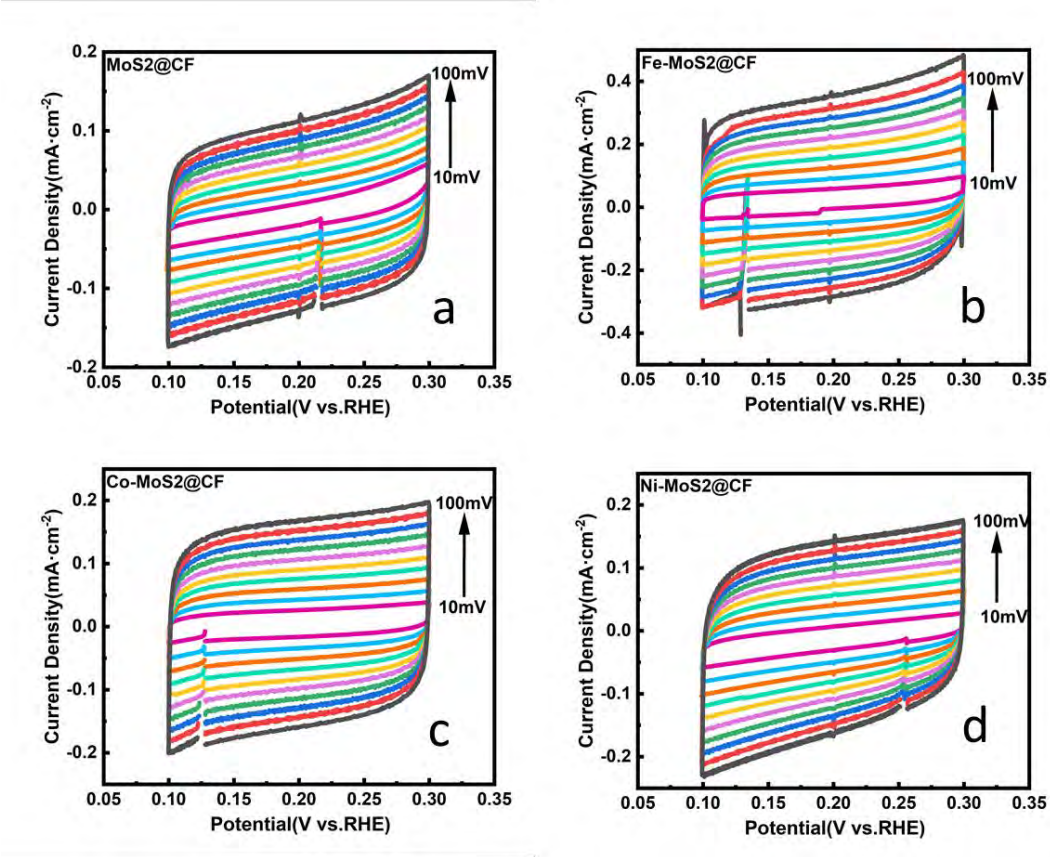

Figure S3. Cyclic voltammograms of MoS_2@GF and X-MoS_2@GF (X = Fe, Co, Ni) in 1.0 mol-L^{-1} KOH solution in the narrow potential range between 0.1 and 0.3 V versus RHE at scanning rates from 10 to 100 mV s^{-1}.

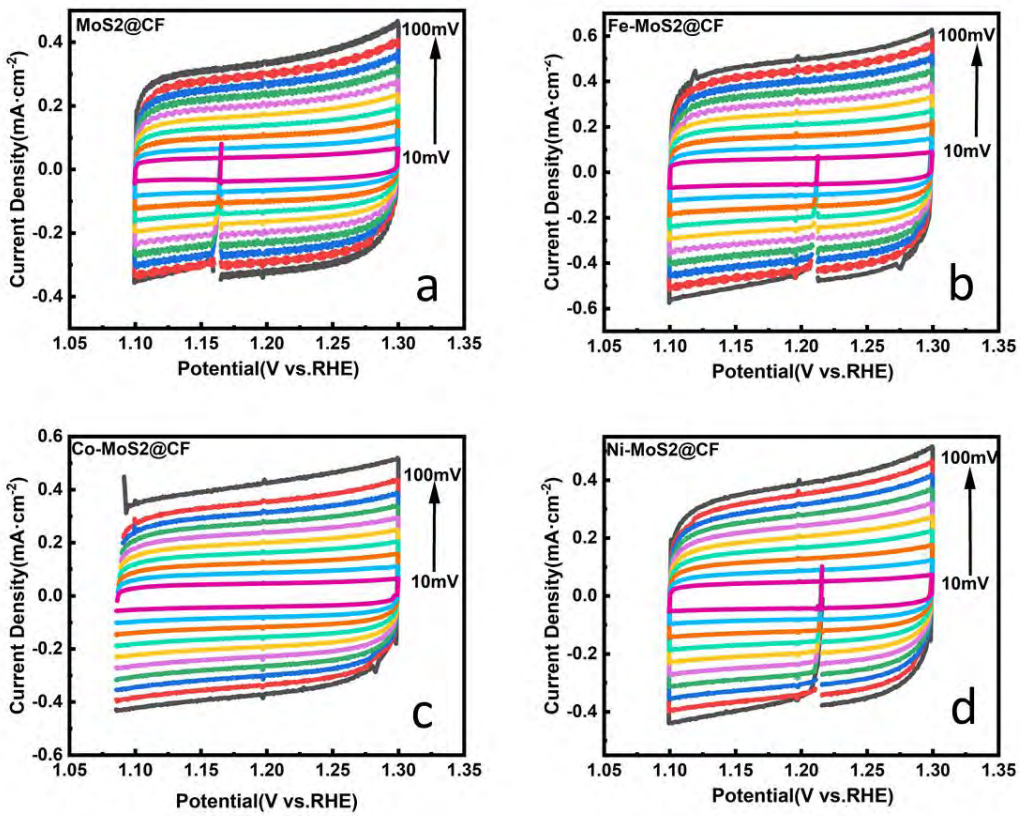

Figure S4. Cyclic voltammograms of MoS_2@GF and X-MoS_2@GF (X = Fe, Co, Ni) in 1.0 mol-L^{-1} KOH solution in the narrow potential range from 1.1 to 1.3 V versus RHE at scanning rates from 10 to 100 mV s^{-1}.

Table S2. Collected data for HER in 1 mol-L^{-1} KOH.

Catalyst	Overpotential (mV) (at 10 mV cm^{-2})	Tafel Slope (mV dec^{-1})	Reference
MoS_2@GF	291.9	89.54	This Work
Fe-MoS_2@GF	71.3	61.55	This Work
Co-MoS_2@GF	83.6	107.07	This Work
Ni-MoS_2@GF	104.5	128.05	This Work
Co-doped MoS_2	90	50	1
FeS_2-MoS_2	136	82	2
Ni-doped MoS_2	98	60	3
1T/2H MoS_2	234	46	4
MoS_2/CNT	290	47	5
MoS_2/RGO	145	41	6
MoS_2/GF	100	39	7
MoS_2/Co_9S_8/Ni_3S_2/Ni	113	85	8
Ni-doped 1T MoS_2	112	48	9
Covalent Cobalt doped MoS_2	132	52	10

Table S3. Collected data for OER in 1 mol-L^{-1} KOH.

Catalyst	Overpotential(mV) (10 mA cm^{-2})	Tafel Slope (mV dec^{-1})	Reference
MoS_2@GF	363.12	177.64	This Work
Fe-MoS_2@GF	221.82	107.08	This Work
Co-MoS_2@GF	289.96	133.13	This Work
Ni-MoS_2@GF	354.27	139.67	This Work
Co-doped MoS_2	190	64	11
Ni-doped MoS_2	320	88	12
Fe-Doped MoS_2	230	79	13
MoS_2@CoNC	257	52	14
1T-MoS_2/CNT	280	N/A	15
Pd@1T-MoS_2	200	N/A	16
Ni-MoS_2-RGO	349	122	17
RGO/MoS_2/Pd	245	42	18
Ni-doped 1T MoS_2	224	54	9
Covalent Cobalt doped MoS_2	350	85	10

References

[1] Dai X, Du K, Li Z, Liu M, Ma Y, Sun H, et al. Co-Doped MoS_2 Nanosheets with the Dominant CoMoS Phase Coated on Carbon as an Excellent Electrocatalyst for

Hydrogen Evolution. ACS Applied Materials & Interfaces. 7(2015)27242-53.
[2] Zhao X, Ma X, Lu Q, Li Q, Han C, Xing Z, et al. FeS_2-doped MoS_2 nanoflower with the dominant 1T-MoS_2 phase as an excellent electrocatalyst for high-performance hydrogen evolution. Electrochimica Acta. 249(2017)72-8.
[3] Zhang J, Wang T, Liu P, Liu S, Dong R, Zhuang X, et al. Engineering water dissociation sites in MoS_2 nanosheets for a GFelerated electrocatalytic hydrogen production. Energy & Environmental Science. 9(2016)2789-93.
[4] Wang D, Zhang X, Bao S, Zhang Z, Fei H, Wu Z. Phase engineering of a multiphasic 1T/2H MoS_2 catalyst for highly efficient hydrogen evolution. Journal of Materials Chemistry A. 5(2017)2681-8.
[5] Huang H, Huang W, Yang Z, Huang J, Lin J, Liu W, et al. Strongly coupled MoS_2 nanoflake-carbon nanotube nanocomposite as an excellent electrocatalyst for hydrogen evolution reaction. Journal of Materials Chemistry A. 5(2017)1558-66.
[6] Li Y, Wang H, Xie L, Liang Y, Hong G, Dai H. MoS_2 Nanoparticles Grown on Graphene: An Advanced Catalyst for the Hydrogen Evolution Reaction. Journal of the American Chemical Society. 133(2011)7296-9.
[7] Zhang N, Gan S, Wu T, Ma W, Han D, Niu L. Growth Control of MoS_2 Nanosheets on Carbon Cloth for Maximum Active Edges Exposed: An Excellent Hydrogen Evolution 3D Cathode. ACS Applied Materials & Interfaces. 7(2015)12193-202.
[8] Yang Y, Yao H, Yu Z, Islam SM, He H, Yuan M, et al. Hierarchical Nanoassembly of MoS2/Co_9S_8/Ni_3S_2/Ni as a Highly Efficient Electrocatalyst for Overall Water Splitting in a Wide pH Range. Journal of the American Chemical Society. 141(2019)10417-30.
[9] Wang G, Zhang G, Ke X, Chen X, Chen X, Wang Y, et al. Direct Synthesis of Stable 1T-MoS_2 Doped with Ni Single Atoms for Water Splitting in Alkaline Media. Small. 18(2022)2107238 (1 of 12)
[10] Xiong Q, Wang Y, Liu P-F, Zheng L-R, Wang G, Yang H-G, et al. Cobalt Covalent Doping in MoS_2 to Induce Bifunctionality of Overall Water Splitting. Advanced Materials. 30(2018)1018450.
[11] Xiong Q, Zhang X, Wang H, Liu G, Wang G, Zhang H, et al. One-step synthesis of cobalt-doped MoS_2 nanosheets as bifunctional electrocatalysts for overall water splitting under both acidic and alkaline conditions. Chemical Communications. 54(2018)3859-62.
[12] Wang Y, Sun W, Ling X, Shi X, Li L, Deng Y, et al. Controlled Synthesis of Ni-Doped MoS_2 Hybrid Electrode for Synergistically Enhanced Water-Splitting Process. Chemistry-A European Journal. 26(2020)4097-103.
[13] Xue J-Y, Li F-L, Zhao Z-Y, Li C, Ni C-Y, Gu H-W, et al. In Situ Generation of Bifunctional Fe-Doped MoS_2 Nanocanopies for Efficient Electrocatalytic Water Splitting. Inorganic Chemistry. 58(2019)11202-9.
[14] Sadighi Z, Liu J, Zhao L, CiuGFi F, Kim J-K. Metallic MoS_2 nanosheets: multifunctional electrocatalyst for the ORR, OER and Li-O_2 batteries. Nanoscale. 10(2018)22549-59.
[15] Ji D, Peng S, Fan L, Li L, Qin X, Ramakrishna S. Thin MoS_2 nanosheets grafted

MOFs-derived porous Co-N-C flakes grown on electrospun carbon nanofibers as self-supported bifunctional catalysts for overall water splitting. Journal of Materials Chemistry A. 5(2017)23898-908.
[16] Peng Q, Shu P, Qi X, Chen Y, Gong X. Solving the Trifunctional Activity Challenge of Catalysts in Unitized Regenerative Fuel Cells via 1T-MoS_2-Coordinated Single Pd Atoms. ACS Omega. 6(2021)4731-8.
[17] Zhao M, Zhou G, Liu X, Shen X, Lv J, Hu C, et al. One Step Hydrothermal Synthesis of Ni-MoS_2-RGO Bifunctional Electrocatalysts for HER and OER. International Journal of Electrochemical Science. 16(2021)210323 (1 to 8).
[18] Pandey A, Mukherjee A, Chakrabarty S, Chanda D, Basu S. Interface Engineering of an RGO/MoS_2/Pd 2D Heterostructure for Electrocatalytic Overall Water Splitting in Alkaline Medium. ACS Applied Materials & Interfaces. 11(2019)42094-42103.

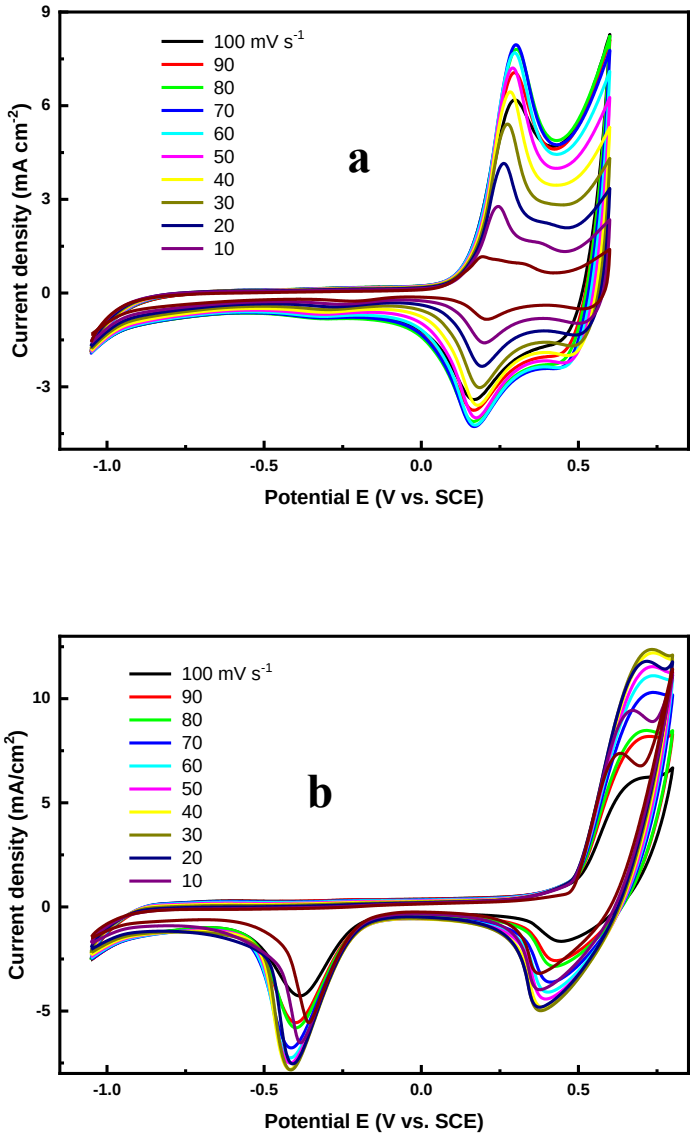

Figure S5. Cyclic voltammograms acquired at scanning rates from 10 to 100 mV-s^{-1} from (a) Co-MoS_2@GF and (b) Ni-MoS_2@GF in 1.0 mol-L^{-1} KOH.

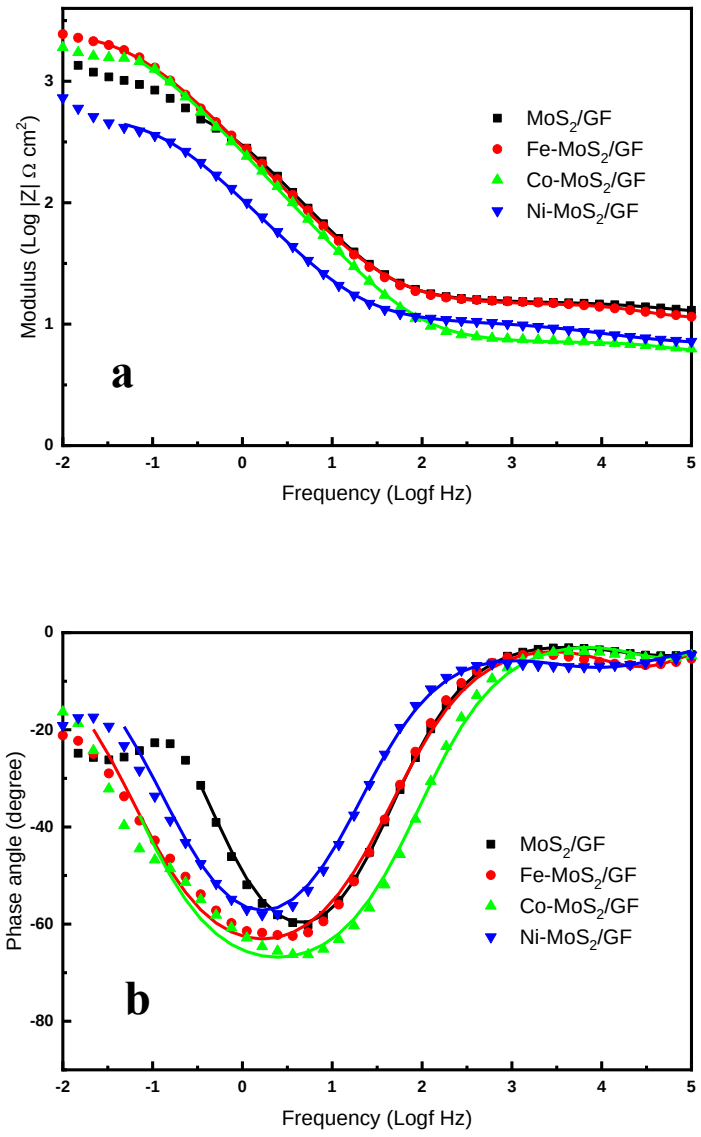

Figure S6. Bode plots of MoS_2@GF and X-MoS_2@GF (X = Fe, Co, Ni) in 1.0 mol-L^{-1} KOH at the open circuit potential. (a) modulus |Z| and (b) phase angle. Experimental (dots) and fitted (solid) data.

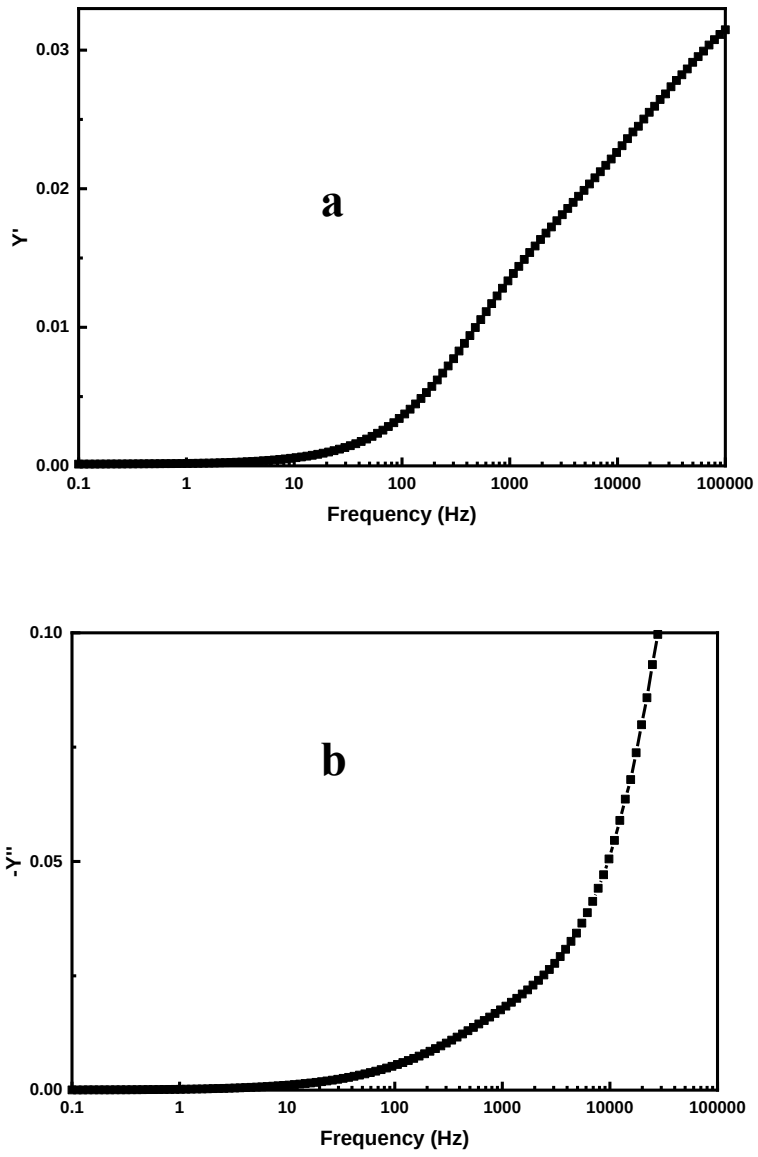

Figure S7. Surface admittance of graphite felt at the open circuit potential in 1.0 mol-L^{-1} KOH solution: (a) Real part and (b) Imaginary part.

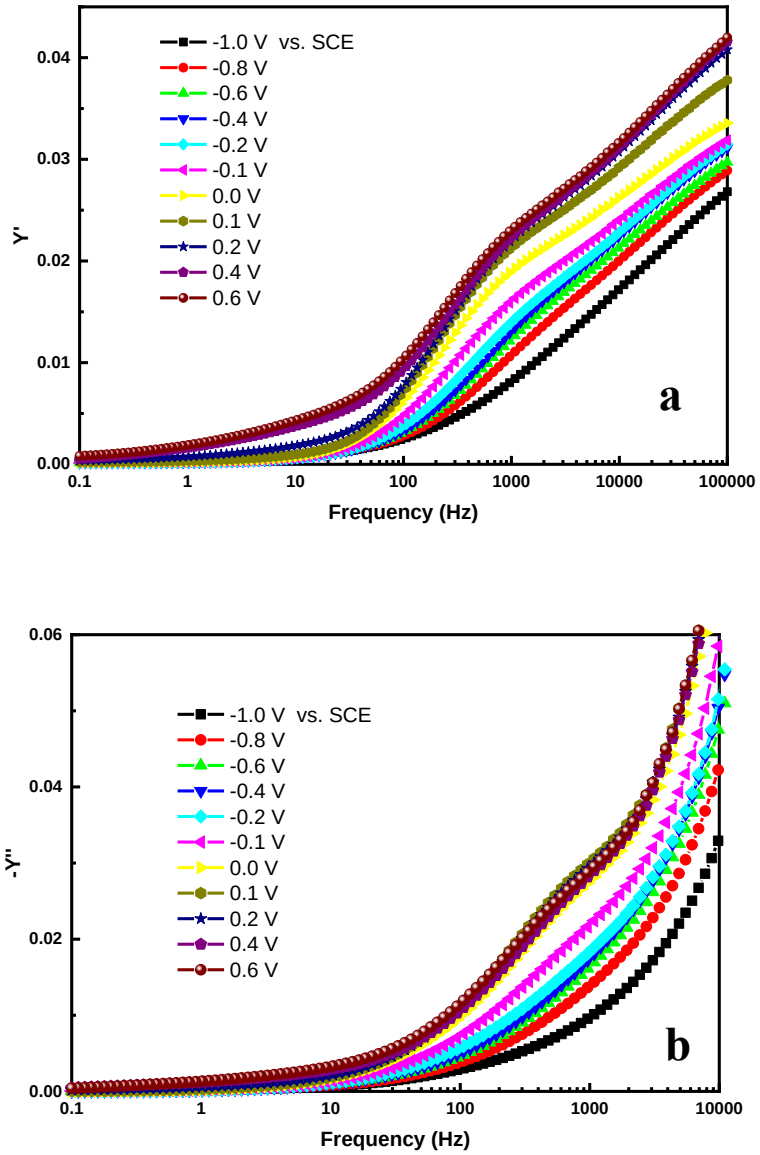

Figure S8. Surface admittance of graphite felt at different potentials in 1.0 mol-L^{-1} KOH: (a) Real part and (b) Imaginary part.